Stress Induced Branching of Growing Crystals on Curved Surfaces

Christian Köhler,[1] Rainer Backofen,[1] and Axel Voigt[1,2]
[1]Institute of Scientific Computing, Technische Universität Dresden, 01062 Dresden, Germany
[2]Dresden Center for Computational Materials Science (DCMS), 01062 Dresden, Germany
(Received 11 November 2015; revised manuscript received 11 January 2016; published 1 April 2016)

If two-dimensional crystals grow on a curved surface, the Gaussian curvature of the surface induces elastic stress and affects the growth pathway. The elastic stress can be alleviated by incorporating defects or, if this is energetically unfavorable, via an elastic instability which leads to anisotropic growth with branched ribbonlike structures. This instability provides a generic route to grow defect-free crystals on curved surfaces. Depending on the elastic properties of the crystal and the geometric properties of the surface, different growth morphologies with two-, four-, and sixfold symmetry develop. Using a phase field crystal type modeling approach, we provide a microscopic understanding of the morphology selection.

DOI: 10.1103/PhysRevLett.116.135502

If a two-dimensional crystal grows on a spherical surface, the symmetry axis of its natural lattice packing is incompatible with the Gaussian curvature of the sphere, inevitably causing elastic stress. The Asaro-Tiller-Grinfeld (ATG) instability [1–3] is a common mechanism to alleviate elastic stress in crystals and is also evident for curvature induced elastic stress [4]. But under growth a different elastic instability occurs, which has been identified by Ref. [5]. It leads to anisotropic growth and defect-free branched ribbonlike structures, which are potentially important for processes involving the ordering of identical subunits in curved space. Examples, as summarized in Ref. [5], are an assembly of viral capsids [6], filament bundle packings [7], formation of molecular monolayers [8], functionalization of nanoparticles [9], and growth of solid domains on vesicles [10–12].

These observed defect-free structures are remarkable, as the ground-state configurations for crystals fully covering the curved surface are not defect-free. Due to topological reasons, they feature crystalline defects, such as disclinations, dislocations, grain boundary scars, and pleats [13–15]. We demonstrate that during growth these ground states are inaccessible for rigid crystals. There, the core energy of the defects is too large, and it is energetically favorable to avoid their incorporation, which leads to the branched structures.

The underlying elastic instability is explained in Ref. [5] by considering an isotropic, circular crystal cap surrounded by melt on a sphere. Using continuum elasticity theory, the energy ΔG_{cap} depends on the crystal cap radius r_0 and the radius of the sphere R [5,16,17]:

$$\Delta G_{\mathrm{cap}} = 2\pi r_0 \gamma + \frac{\pi}{384} Y \frac{r_0^6}{R^4} - \pi \Delta E r_0^2, \tag{1}$$

where Y is the two-dimensional Young's modulus of the crystal. ΔE is the energy difference between crystal and melt, and γ is the line tension of the crystal melt interface. Equation (1) has a global energy minimum at a critical cap size r_c (see Fig. 1). Therefore, isotropic or circular growth of the crystal beyond r_c is energetically prohibited. To grow further, the crystal changes into an anisotropic ribbon shape. The energy of a ribbon of length l and width w on the surface of a sphere is [16,17]

$$\Delta G_{\mathrm{rib}} = 2\gamma(l+w) + \frac{9}{5120} Y \frac{w^5 l}{R^4} - \Delta E l w. \tag{2}$$

For fixed width w the strain energy increases only linearly in l and thus allows for further growth.

However, this argumentation is only valid for rigid crystals as it neglects the possibility to incorporate defects. Soft crystals might never reach the critical size r_c, as incorporation of defects might already be energetically favored over a defect-free, stressed configuration for smaller crystals. In order to account for defect formation, we explore the growth routes for crystals on curved surfaces using a microscopic elastic theory. The theory is based on the phase-field crystal (PFC) model [18,19] (see Ref. [20] for a review on the modeling approach and its

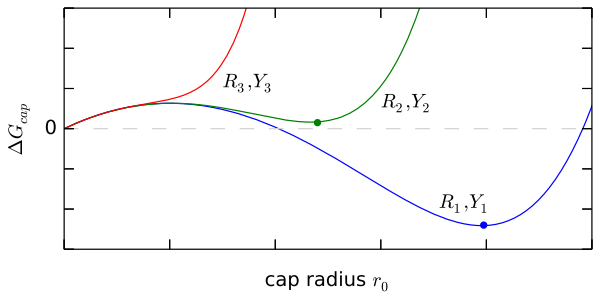

FIG. 1. Qualitative behavior of the energy of a crystal cap on a spherical surface, Eq. (1). Shown are the energies for decreasing surface radii $R_1 > R_2 > R_3$ and increasing Young's moduli $Y_1 < Y_2 < Y_3$ with the energy minima marked by dots. ΔE and γ are fixed.

wide applicability in condensed and soft matter physics). Using the derivation of the model from classical dynamic density functional theory [21–23], we consider a higher order PFC model as proposed in Refs. [24,25]. The additional degrees of freedom allow us to independently choose, e.g., the elastic constants of the crystal and the energy difference between liquid and solid phases. These degrees of freedom are mandatory, as we aim for a description of crystals with varying rigidity. The PFC model is a conserved evolution equation for the reduced particle density ψ and reads

$$\partial_t \psi = \Delta_\Gamma \frac{\delta F[\psi]}{\delta \psi}, \tag{3}$$

with an energy functional

$$F[\psi] = \int_\Gamma \left[\frac{\psi}{2} \omega(\Delta_\Gamma)\psi + \frac{\psi^4}{4} \right] d\Gamma, \tag{4}$$

which is formulated here on the spherical surface Γ, using the surface Laplacian Δ_Γ (see Refs. [23,26,27]). Using the notation of Refs. [24,25], we define

$$\omega(\Delta_\Gamma) = \epsilon - \Lambda\left(1 + \frac{\Delta_\Gamma}{k_m^2}\right)^2 - E_B\left(1 + \frac{\Delta_\Gamma}{k_m^2}\right)^4,$$
$$\Lambda = -\frac{k_m^2 \gamma_8}{8}, \qquad E_B = -(C_0 - \epsilon + \Lambda). \tag{5}$$

The parameter ϵ is the undercooling of the system, k_m the equilibrium wave number of the crystal, γ_8 the curvature of the energy kernel $\hat{\omega}$ in Fourier space at k_m, and C_0 the energy of the liquid phase (see Fig. 2 for details). Depending on these parameters and the average density of the system $\bar{\psi}$, the functional Eq. (4) is minimized by periodic and/or constant solutions, modeling a crystal and its melt, respectively.

Within the one-mode approximation in flat space [19], the periodic solution is given in the (x, y) plane by

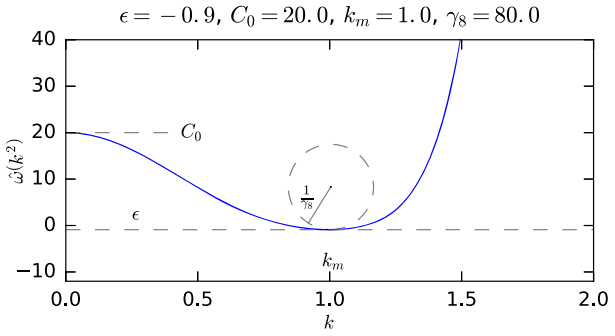

FIG. 2. Parametrization of the energy kernel $\omega(\Delta_\Gamma)$ in Fourier space.

$$\psi_t = A_t \left[\cos(q_t x) \cos\left(\frac{q_t}{\sqrt{3}} y\right) - \frac{1}{2} \cos\left(\frac{2q_t}{\sqrt{3}} y\right) \right] + \bar{\psi} \tag{6}$$

with the equilibrium wave number q_t and amplitude A_t defined as

$$q_t = \frac{\sqrt{3}|k_m|}{2}, \qquad A_t = \frac{4\bar{\psi}}{5} + \frac{4\sqrt{3}}{15}\sqrt{-12\bar{\psi}^2 - 5\epsilon}. \tag{7}$$

This one-mode approximation can be used to compute the two-dimensional Young's modulus Y and the solid-liquid energy difference ΔE,

$$Y = \frac{1}{8}\gamma_8 A_t^2 k_m^2, \tag{8}$$

$$\Delta E = \frac{45}{512} A_t^4 - \frac{3}{16}\bar{\psi} A_t^3 + \left(\frac{9}{16}\bar{\psi}^2 + \frac{3}{16}\epsilon\right) A_t^2. \tag{9}$$

We introduce a length scale $k_m = 1$ and ensure a large crystal-melt coexistence regime by fixing $C_0 = 20$ and $\epsilon = -0.9$. We are interested in finite-size crystals. Moreover, these should grow only slowly in order to avoid Mullins-Sekerka–type instabilities [28]. We realize such crystals by choosing the average densities $\bar{\psi} = -0.585$, $\bar{\psi} = -0.590$, and $\bar{\psi} = -0.595$ close to the coexistence regime (see Supplemental Material Ref. [29]).

Neglecting the line tension γ in Eq. (1) renders the critical radius

$$r_c = \left(128 \frac{\Delta E}{Y}\right)^{(1/4)} R \tag{10}$$

a function of γ_8 [via Eq. (8)], the remaining adjustable parameter of the PFC model.

We numerically solve the eighth-order partial differential equation (3) using a semi-implicit Euler scheme [30] combined with a basis decomposition of the density field ψ into spherical harmonics [31]. The initial condition is set using the one-mode approximation with fixed amplitude $A_t = 0.67$, resulting from our previously chosen values of ϵ and $\bar{\psi}$, and restricted to a cap of size $r_0 = 40$. The remainder of the spherical surface is covered by the surrounding melt. In order to realize setups with different critical cap sizes r_c, we vary the defining parameters $\gamma_8 = 20, \ldots, 160$ and $R = 40/q_t, \ldots, 120/q_t$ in steps of $\Delta\gamma_8 = 10$ and $\Delta R = 10/q_t$. This also renders the crystals sufficiently rigid to realize defect-free growth. We first focus on the mesoscopic shapes of the crystals and explain the microscopic origin of the shape selection afterwards. The mesoscopic results are summarized in Fig. 3. Besides the parameter setting for which the initial crystal melts [white circles in Fig. 3(b)], the crystal cap isotropically grows in a perfect triangular lattice with sixfold symmetry

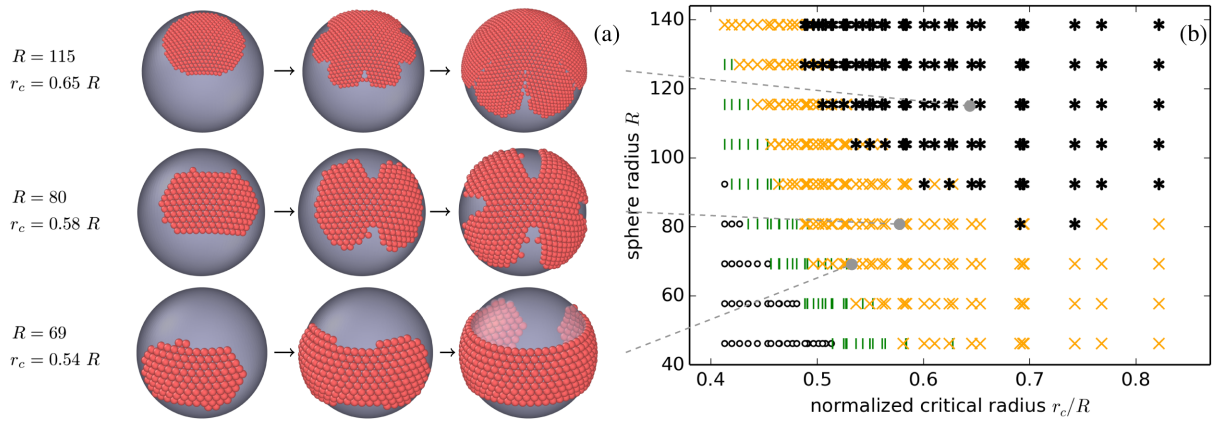

FIG. 3. (a) Temporal evolution (from left to right) of different growth patterns of crystals on a sphere. Top row: Sixfold branching; middle row: fourfold branching; bottom row: formation of a single ribbon. For illustration purposes, the maxima in the density field ψ are displayed as particles, using OVITO [32]. (b) State diagram of the growth patterns. Depending on the sphere radius R and the critical cap size r_c, sixfold branching (black stars), fourfold branching (yellow crosses), or ribbon formation (green vertical dashes) is realized. The white circles mark parameter combinations for which the initial condition decays into a constant solution (melt) (compare Fig. 1).

until it reaches its critical size. In accordance with the continuum elastic theory [5], further growth leads to a morphological transition. However, we encounter different morphological patterns, shown in Fig. 3(a). The first one develops six branches, starting at the corners of the underlying hexagonal crystal structure. In the second growth pattern, the cap structure transforms into a short ribbon structure which subsequently branches, forming four ribbons. Finally, the third growth route features a transition into a single ribbon, which only increases its length upon temporal evolution. Figure 3(b) shows the realized growth patterns for different sphere radii R and critical radii r_c. Using r_c/R as a parameter leads to a clear separation of the different growth morphologies. A transition from sixfold branching (black stars) to fourfold branching (yellow crosses) and twofold branching (green vertical dashes) for decreasing r_c/R or R is evident. In accordance with our results, Meng *et al.* [5] experimentally found similar branched structures for $r_c/R \approx 0.4$–0.5 and $R \approx 110/q_t$. However, they attribute branching to the equivalence of growth directions or coalescence of ribbons. Our results demonstrate that the elastic instability alone may lead to branching.

What triggers the different growth morphologies? Let us consider a sphere with $R = 110/q_t$ for fixed $\bar{\psi} = -0.595$. We choose the decreasingly rigid crystals with $\gamma_8 = 160$, $\gamma_8 = 140$, and $\gamma_8 = 80$ as representatives for the growth patterns of twofold (ribbon), fourfold, and sixfold branching. For the explanation we use a microscopic picture with discrete particles. Now, crystal growth can be considered as a series of attachment events of particles at energetically favorable open lattice sites [33–36]. As kinetic effects are excluded, the next particle will attach at the site with the maximal number of bonds with the least elastic stress. As we are only interested in energy differences, we consider the energy density in Eq. (4) evaluated in the maxima of the density field ψ as an indicator for the elastic stress.

Starting from the seed crystal with its perfect sixfold symmetry, the crystal grows by adding particles on the facets, to which new particles attach until the next layer of particles is closed. After each attachment of a particle, the crystal relaxes elastically. Figure 4 illustrates the attachment and relaxation process by plotting the energy density on the facet sites. The colors of the particles on the left represent the energy density configuration on the facets of the growing crystal before and after the elastic relaxation of the respective layer. The right part shows the facet of the last growing layer before symmetry breaks. There, the energy density configuration is supplemented by the maximum, average, and minimum values, and the corresponding time scales are given. The energy density value in the corners evolves similarly (see Supplemental Material Ref. [29]). While the attachment and relaxation process is basically the same for all three configurations, the energy differences and the distribution along the facets differ. For $\gamma_8 = 160$ and 140 the maximum values before and after relaxation are always at the ends of the facet, and a minimum is found in the middle. For $\gamma_8 = 80$ the situation qualitatively changes. For larger facets two minima develop together with two local maxima at the ends of the facet, and a global maximum arises in the middle of the facet.

Once the critical radius r_c is reached, the asymmetry develops in the local energy density during the relaxation process. This relaxation takes longer for more rigid crystals (see time scales in Fig. 4 and movies in Supplemental Material Ref. [29]). Figure 5 shows the energy density at each particle at the crystal-melt interface after relaxation of the latest symmetric morphology. For the softest case of $\gamma_0 = 80$, the sixfold symmetry is conserved and all six corners are the energetically most favorable sites. For

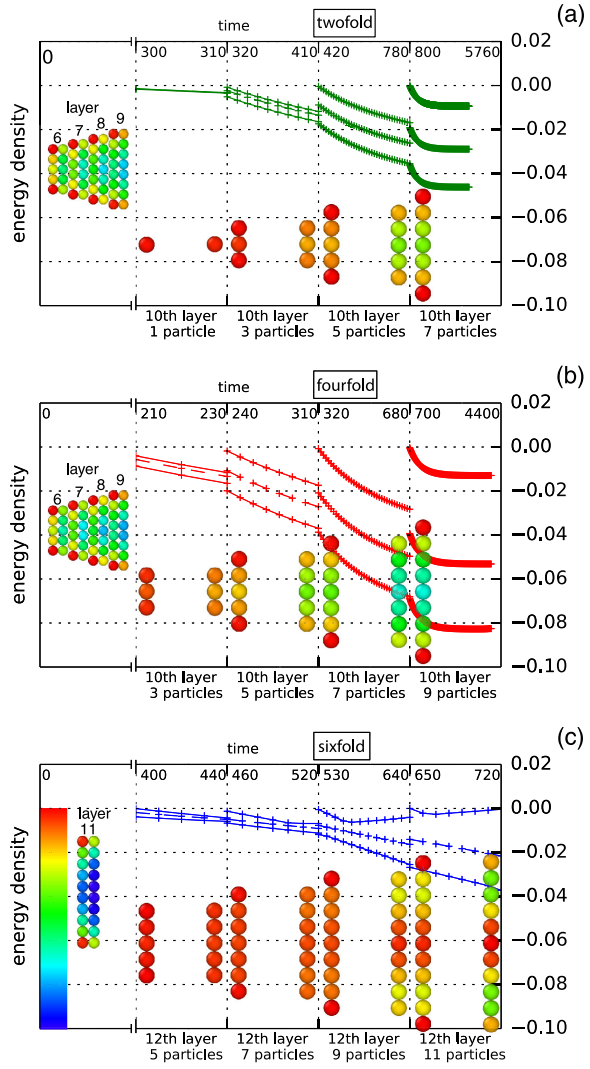

FIG. 4. Averaged energy density evaluated at the facets for each layer until the symmetry breaks. We show the maximum, average, and minimum values along the last growing layer. The (+) corresponds to the equidistant time steps. In addition, the facet configuration, together with the energy density, is shown after the attachment and relaxation process, for (a) $\gamma_8 = 160$, (b) $\gamma_8 = 140$, and (c) $\gamma_8 = 80$. The colors of the particles indicate the energy density [from low (blue) to high (red) as shown by the color bar in (c)].

$\gamma_8 = 140$, we observe an asymmetry with four facets being energetically favorable over the remaining two facets and six corners. The most rigid case of $\gamma_8 = 160$ shows an asymmetry of two corners being energetically cheaper than the other four corners or six facets. Similarly, the energetically most unfavorable sites are found in the middle of the facets ($\gamma_8 = 80$) or at the ends of two opposing facets ($\gamma_8 = 140$, even more pronounced for $\gamma_8 = 160$). The time evolution in Fig. 6 starts from this configuration (left) and shows the next rearrangement step which selects the morphology (middle) and a later configuration with the developed twofold, fourfold, or sixfold symmetry (right).

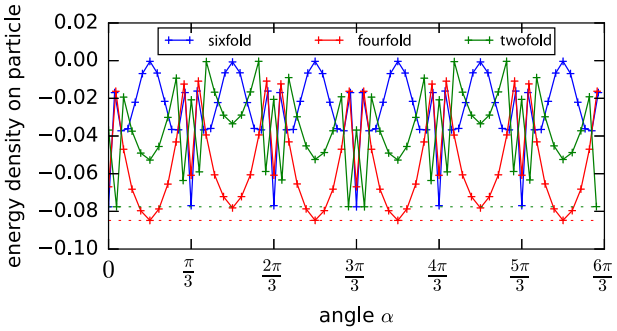

FIG. 5. Energy density over each particle on the crystal-melt interface, plotted as a function of angle and evaluated at the last configuration shown in Fig. 4, also corresponding to the first frame shown in Fig. 6. The developing twofold, fourfold, and sixfold symmetry is already visible.

The symmetry breaking in the morphology is, in all cases, associated with a detachment (attachment) process of particles at the energetically most unfavorable (favorable) sites. For $\gamma_8 = 160$, detachment happens at the ends of two opposite facets. The next attachment process is at the corners, which are not associated with these two facets, leading to the twofold symmetry. For $\gamma_8 = 140$, the symmetry breaking happens slightly differently. Because

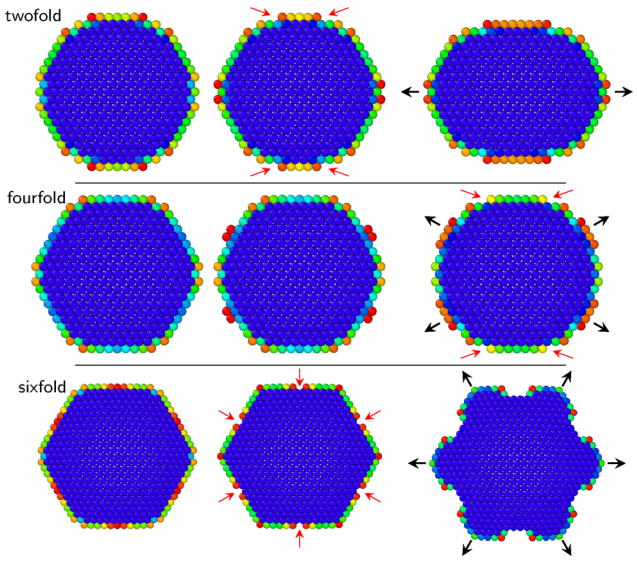

FIG. 6. Growth morphology and energy density at the largest symmetric configuration after elastic relaxation (left). The color indicates the energy density (blue-low, red-high) and is the same as in Fig. 4. We show the configuration after further attachment or reconfiguration (middle) and developed morphology (right). The detachment events are indicated by red arrows, and the asymmetric growth direction by black arrows. The top row shows the evolution for $\gamma_8 = 160$ leading to twofold symmetry, the middle row the evolution for $\gamma_8 = 140$ leading to fourfold symmetry, and the bottom row the evolution for $\gamma_8 = 80$ leading to sixfold symmetry. The whole evolutions are provided as movies in Supplemental Material Ref. [29].

of the energy density minima at four facets, formation of the new layer happens there first. But instead of starting a new layer on the two remaining facets, particles get detached from the existing layer on these facets and attached on the already growing layers on the other four facets, leading to the fourfold symmetry. Only for $\gamma_8 = 80$ does the configuration stay symmetric. But the maximum energy density is found in the center points of the facets, leading to a detachment process there and attachment at the energetically more favorable corners. This initiates the sixfold symmetry with branches developing in each corner. Only very soft crystals remain in a compact caplike shape. Here, the branches immediately grow together, leaving behind scarlike structures. In the Supplemental Material Ref. [29] a movie is provided showing the simulation results for $\gamma_8 = 0.1$.

To conclude, anisotropic crystal growth is shown as the result of a geometric constraint of Gaussian curvature. We have shown that the developing morphology thereby strongly depends on the elastic properties of the crystal leading to twofold, fourfold, or sixfold branched structures. These patterns are a result of broken symmetry in the elastic energy on the microscopic particle scale.

This work was financially supported by DFG through SPP 1296 within Project No. Vo899-7. We used computing resources provided by Jülich Supercomputing Center within Project No. HDR06.

[1] R. Asaro and W. Tiller, Metall. Trans. **3**, 1789 (1972).
[2] M. A. Grinfield, Sov. Phys. Dokl. **31**, 831 (1986).
[3] D. Srolovitz, Acta Metall. **37**, 621 (1989).
[4] C. Köhler, R. Backofen, and A. Voigt, Europhys. Lett. **111**, 48006 (2015).
[5] G. Meng, J. Paulose, D. R. Nelson, and V. N. Manoharan, Science **343**, 634 (2014).
[6] W. Roos, R. Bruinsma, and G. Wuite, Nat. Phys. **6**, 733 (2010).
[7] I. R. Bruss and G. Grason, Proc. Natl. Acad. Sci. U.S.A. **109**, 10781 (2012).
[8] G. DeVries, M. Brunnbauer, Y. Hu, A. Jackson, B. Long, B. Neltner, O. Uzun, B. Wunsch, and F. Stellacci, Science **315**, 358 (2007).
[9] H. Bao, W. Peukert, and R. Klupp, Adv. Mater. **23**, 2644 (2011).
[10] J. Korlach, P. Schwille, W. Webb, and G. Feigenson, Proc. Natl. Acad. Sci. U.S.A. **96**, 8461 (1999).
[11] A. Bandekar and S. Sofou, Langmuir **28**, 4113 (2012).
[12] T. Witkowski, R. Backofen, and A. Voigt, Phys. Chem. Chem. Phys. **14**, 14509 (2012).
[13] A. R. Bausch, M. J. Bowick, A. Cacciuto, A. D. Dinsmore, M. F. Hsu, D. R. Nelson, M. G. Nikolaides, A. Travesset, and D. A. Weitz, Science **299**, 1716 (2003).
[14] P. Lipowsky, M. J. Bowick, J. H. Meinke, D. R. Nelson, and A. R. Bausch, Nat. Mater. **4**, 407 (2005).
[15] W. T. M. Irvine, V. Vitelli, and P. M. Chaikin, Nature (London) **468**, 947 (2010).
[16] S. Schneider and G. Gompper, Europhys. Lett. **70**, 136 (2005).
[17] C. Majidi and R. S. Fearing, Proc. R. Soc. A **464**, 1309 (2008).
[18] K. Elder, M. Katakowski, M. Haataja, and M. Grant, Phys. Rev. Lett. **88**, 245701 (2002).
[19] K. Elder and M. Grant, Phys. Rev. E **70**, 051605 (2004).
[20] H. Emmerich, H. Löwen, R. Wittkowski, T. Gruhn, G. I. Tóth, G. Tegze, and L. Gránásy, Adv. Phys. **61**, 665 (2012).
[21] K. Elder, N. Provatas, J. Berry, and P. Stefanovic, Phys. Rev. B **75**, 064107 (2007).
[22] S. van Teeffelen, R. Backofen, A. Voigt, and H. Löwen, Phys. Rev. E **79**, 051404 (2009).
[23] R. Backofen, M. Gräf, D. Potts, S. Praetorius, A. Voigt, and T. Witkowski, Multiscale Model. Simul. **9**, 314 (2011).
[24] A. Jaatinen, C. Achim, K. Elder, and T. Ala-Nissila, Phys. Rev. E **80**, 031602 (2009).
[25] A. Jaatinen and T. Ala-Nissila, Phys. Rev. E **82**, 061602 (2010).
[26] R. Backofen, A. Voigt, and T. Witkowski, Phys. Rev. E **81**, 025701 (2010).
[27] V. Schmid and A. Voigt, Soft Matter **10**, 4694 (2014).
[28] W. W. Mullins and R. F. Sekerka, J. Appl. Phys. **35**, 444 (1964).
[29] See Supplemental Material at http://link.aps.org/supplemental/10.1103/PhysRevLett.116.135502 for phase diagram, energy density at corners and movies showing the developing instabilities.
[30] R. Backofen, A. Rätz, and A. Voigt, Philos. Mag. Lett. **87**, 813 (2007).
[31] N. Schaeffer, Geochem. Geophys. Geosyst. **14**, 751 (2013).
[32] A. Stukowski, Model. Simul. Mater. Sci. Eng. **18**, 015012 (2010).
[33] B. Orr, D. Kessler, C. Snyder, and L. Sander, Europhys. Lett. **19**, 33 (1992).
[34] C. Lam, C. Lee, and L. Sander, Phys. Rev. Lett. **89**, 216102 (2002).
[35] G. Russo and P. Smereka, J. Comput. Phys. **214**, 809 (2006).
[36] T. Schulze and P. Smereka, J. Mech. Phys. Solids **57**, 521 (2009).